Seventh International Conference on Computational Fluid Dynamics (ICCFD7), Big Island, Hawaii, July 9-13, 2012

ICCFD7-2201

LES modeling with high-order flux reconstruction and spectral difference schemes

G. Lodato and A. Jameson
Corresponding author: glodato@stanford.edu

Department of Aeronautics and Astronautics,
Stanford University, Stanford, CA 94305, USA.

Abstract: The combination of the high-order unstructured flux reconstruction and spectral difference spatial discretization schemes with sub-grid scale modeling for large-eddy simulation is investigated with particular focus on the consistent implementation of a structural mixed model based on the scale similarity hypothesis. The difficult task of deriving a consistent formulation for the discrete filter within hexahedral elements of arbitrary order led to the development of a new class of three-dimensional constrained discrete filters. Results from different canonical tests cases, including turbulent channel flows and turbulent wakes behind bluff bodies at various Reynolds numbers, are presented. The numerical experiments suggest that the results are sensitive to the use of an sub-grid scale closure, even when a high-order numerical scheme is used, especially when the grid resolution is kept relatively low. The use of the similarity mixed formulation proved to be particularly accurate in reproducing sub-grid scale interactions, confirming that its well-known potential can be realized in conjunction with state-of-the-art high-order numerical schemes.

Keywords: High-Order Methods, Large-Eddy Simulation, Sub-Grid Scale Modeling.

1 Introduction

Notwithstanding the considerable effort which has been devoted to the development of accurate and relatively reliable Sub-Grid Scale (SGS) models for Large-Eddy Simulation (LES), the underlying numerical methods, which are available within the framework of industrial computational fluid dynamics applications generally rely upon highly dissipative schemes. The inherent numerical dissipation introduced by such numerical schemes limits their ability to correctly represent the whole spectrum resolved in LES.

Hence it is necessary to combine high order numerical schemes with advanced SGS modeling techniques in order for LES to become a valuable and reliable tool for fundamental flow physics and industrial applications. Unfortunately, most of the available high-order numerical schemes are designed to be used on cartesian or very smooth structured curvilinear meshes and therefore they are inadequate to simulate turbulent flows over complex geometries. In the current work, a high-order unstructured solver is combined with an explicit filtering LES method, thus allowing highly accurate turbulent flow computations on realistic geometries that were previously only possible with low-order schemes.

High-order numerical schemes for solving the compressible Navier-Stokes equations on unstructured grids have been widely studied during the last decade. By far the most mature and widely used of these schemes are based on the Discontinuous Galerkin (DG) method [1, 2]. However, several alternative high-order methods have been recently proposed, including Spectral Difference (SD) type schemes [3–9], which potentially offer increased efficiency compared with DG methods (as well as being simpler to implement). The SD method has been successfully applied to viscous compressible flows with shocks [10], implicit LES of turbulent channel flow [11], and flow around circular cylinders [12, 13], as well as, transitional flows over an SD7003 airfoil [14]. The combination of the SD method with SGS modeling techniques for explicit LES, on the other hand, has not been widely studied. Parsani et al. [15] obtained encouraging results using the Wall-Adapting Local

Eddy-viscosity (WALE) model [16] but their analysis was restricted to two-dimensional flows. A three-dimensional computation of turbulent flow in a muffler at $Re = 46\,650$ was also reported [17].

In the context of the SD method for three-dimensional unstructured hexahedral grids, the present study addresses the implementation of a structural SGS model based on the scale similarity assumption [18], namely, the WALE Similarity Mixed model (WSM) proposed by Lodato et al. [19]. To the authors' knowledge, this represents the first implementation of a structural SGS model in a three-dimensional solver that uses the SD method. Moreover, the proposed implementation of a constrained discrete filter of arbitrary order for the SD method will be suitable for a broad class of numerical schemes based on the discontinuous finite element representation of the solution, such as the family of energy stable schemes that can be obtained within the unifying Flux Reconstruction (FR) framework [4, 20–28].

2 Mathematical formulation

2.1 The numerical scheme

In the present work, the Navier-Stokes equations are solved using the high-order unstructured SD method for spatial discretization, which is here adopted as representative of the more general family of energy stable FR schemes. Note that, as mentioned in the introduction, all the results reported below can be extended to the FR methodology (as well as to other discontinuous finite element schemes) in a straightforward way. The formulation of the equations on hexahedral grids is similar to the formulation by Sun et al. [7], which will be summarized below for completeness. After introducing the *bar* filter operator and the density-weighted Favre filter operator *tilde*, the unsteady compressible Navier-Stokes equations in conservative form are written as

$$\frac{\partial \overline{\boldsymbol{U}}}{\partial t} + \frac{\partial \overline{\boldsymbol{F}}^k}{\partial x_k} = \boldsymbol{0}, \tag{1}$$

where $\overline{\boldsymbol{U}} = \begin{pmatrix} \overline{\rho} & \overline{\rho u_1} & \overline{\rho u_2} & \overline{\rho u_3} & \overline{\rho e} \end{pmatrix}^{\mathrm{T}}$ is the vector of conservative variables, and $\overline{\boldsymbol{F}}^k = \overline{\boldsymbol{F_I}}^k - \overline{\boldsymbol{D}}^k$ accounts for the inviscid and viscous flux vectors, which are defined as

$$\overline{\boldsymbol{F_I}}^k = \begin{pmatrix} \overline{\rho u}_k \\ \overline{\rho u}_1 \widetilde{u}_k + \delta_{1k}\overline{\varpi} \\ \overline{\rho u}_2 \widetilde{u}_k + \delta_{2k}\overline{\varpi} \\ \overline{\rho u}_3 \widetilde{u}_k + \delta_{3k}\overline{\varpi} \\ (\overline{\rho e} + \overline{\varpi})\widetilde{u}_k \end{pmatrix}, \quad \overline{\boldsymbol{D}}^k = \begin{pmatrix} 0 \\ 2\overline{\mu}\widetilde{A}_{1k} + \tau^{\mathrm{d}}_{1k} \\ 2\overline{\mu}\widetilde{A}_{2k} + \tau^{\mathrm{d}}_{2k} \\ 2\overline{\mu}\widetilde{A}_{3k} + \tau^{\mathrm{d}}_{3k} \\ 2\overline{\mu}\widetilde{u}_j \widetilde{A}_{kj} + \frac{\overline{\mu} c_p}{\mathrm{Pr}} \frac{\partial \widetilde{\vartheta}}{\partial x_k} + q_k \end{pmatrix}, \tag{2}$$

where ρ is the fluid's density, u_k is the velocity vector, e is the total energy (internal + kinetic), μ is the dynamic viscosity, A_{ij} is the deviator of the deformation tensor, c_p is the specific heat capacity at constant pressure and Pr is the Prandtl number. In particular, $\overline{\varpi}$ and $\widetilde{\vartheta}$ are the filtered *macro-pressure* and *macro-temperature* [19, 29], these quantities being related by the usual equation of state, i.e., $\overline{\varpi} = \overline{\rho} R \widetilde{\vartheta}$. τ_{ij} and q_k in Eq. (2) represent the usual unclosed SGS terms (note that the superscript 'd' refers to the deviatoric part of the relevant tensor).

To achieve an efficient implementation, all elements in the physical domain are transformed to a standard cubic element described by local coordinates $\boldsymbol{\xi} = (\xi_1, \xi_2, \xi_3)$, with $\boldsymbol{\xi} \in [0:1]^3$. The governing equations in the physical domain are then transferred into the computational domain, and they take the form

$$\frac{\partial \overline{\boldsymbol{\mathcal{U}}}}{\partial t} + \frac{\partial \overline{\boldsymbol{\mathcal{F}}}^k}{\partial \xi_k} = \boldsymbol{0}, \tag{3}$$

where

$$\overline{\boldsymbol{\mathcal{U}}} = |\det(\boldsymbol{J})| \overline{\boldsymbol{U}} \quad \text{and} \quad \overline{\boldsymbol{\mathcal{F}}}^k = |\det(\boldsymbol{J})| \frac{\partial \xi_k}{\partial x_j} \overline{\boldsymbol{F}}^j, \tag{4}$$

and $\det(\boldsymbol{J})$ represents the determinant of the Jacobian matrix $\boldsymbol{J}_{ij} = \partial x_i / \partial \xi_j$.

Within each standard element, two sets of points are defined, namely the solution points and the flux

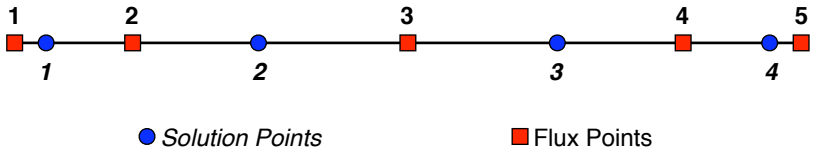

Figure 1: Schematic representation of the one dimensional distribution of solution and flux points within the SD element for $N = 4$.

points, as schematically illustrated in figure 1 for a one-dimensional element. In order to construct a degree $(N-1)$ polynomial for each coordinate direction, solution at N points are required. These N points in 1D are chosen to be the Gauss-Legendre quadrature points, whereas the flux points were selected to be the Gauss-Legendre quadrature points of order $N-1$ plus the two end points 0 and 1. Using the N solution points and the $N+1$ flux points, polynomials of degree $N-1$ and N, respectively, can be built using Lagrange bases defined as

$$h_i(\xi) = \prod_{s=1, s\neq i}^{N} \left(\frac{\xi - \xi_s}{\xi_i - \xi_s} \right), \quad \text{and} \quad l_{i+1/2}(\xi) = \prod_{s=0, s\neq i}^{N} \left(\frac{\xi - \xi_{s+1/2}}{\xi_{i+1/2} - \xi_{s+1/2}} \right). \tag{5}$$

The reconstructed solution for the conserved variables in the standard element is then obtained as the tensor product of the three one-dimensional polynomials,

$$\overline{\boldsymbol{U}}(\boldsymbol{\xi}) = \sum_{k=1}^{N} \sum_{j=1}^{N} \sum_{i=1}^{N} \frac{\overline{\boldsymbol{U}}_{i,j,k}}{|J_{i,j,k}|} h_i(\xi_1) h_j(\xi_2) h_k(\xi_3), \tag{6}$$

where i, j and k are the indices of the solution points within each standard element. A similar reconstruction is adopted for the resolved fluxes $\overline{\boldsymbol{\mathcal{F}}}^k$.

The reconstructed fluxes are only element-wise continuous, but discontinuous across cell interfaces. For the inviscid flux, a Riemann solver is employed to compute a common flux at cell interfaces to ensure conservation and stability. In the current implementation, the Roe solver [30] with entropy fix [31] was used. The left and right states here represent the solution on both sides of the shared edge flux point. The viscous flux is a function of both the conserved variables and their gradients, therefore, the solution gradients have to be calculated at the flux points. The average approach described by Sun et al. [7] is used to compute the viscous fluxes.

2.2 LES modeling approach

In order to close the SGS terms a structural model based on the scale similarity assumption [18, 32, 33] is adopted. In the perspective of developing a similarity mixed formulation [33–40] with correct near-wall scaling, a WALE formulation [16] for the eddy-viscosity term was recently proposed by Lodato et al. [19]:

$$\tau_{ij}^{\mathrm{d}} = 2\overline{\rho}\nu_{\mathrm{sgs}}\widetilde{A}_{ij} - \overline{\rho}\big(\widehat{\widetilde{u}_i\widetilde{u}_j} - \widehat{\widetilde{u}}_i\widehat{\widetilde{u}}_j\big)^{\mathrm{d}}, \tag{7}$$

$$q_k = \gamma\overline{\rho}\kappa_{\mathrm{sgs}}\frac{\partial \widetilde{e_I}}{\partial x_k} - \gamma\overline{\rho}\big(\widehat{\widetilde{e_I}\widetilde{u}_k} - \widehat{\widetilde{e_I}}\widehat{\widetilde{u}}_k\big), \tag{8}$$

where $\widetilde{e_I}$ is the resolved internal energy and the *hat* operator represents filtering at cutoff length $\alpha\Delta_{\mathrm{g}}$, with $\alpha \geq 1$ and sufficient localization in physical space [32]. the SGS kinematic viscosity, ν_{sgs}, and thermal diffusivity, κ_{sgs}, are computed as [16]

$$\nu_{\mathrm{sgs}} = C_{\mathrm{w}}^2\Delta_{\mathrm{g}}^2\frac{(\widetilde{s}_{ij}^{\mathrm{d}}\widetilde{s}_{ij}^{\mathrm{d}})^{3/2}}{(\widetilde{A}_{ij}\widetilde{A}_{ij})^{5/2} + (\widetilde{s}_{ij}^{\mathrm{d}}\widetilde{s}_{ij}^{\mathrm{d}})^{5/4}}, \quad \text{and} \quad \kappa_{\mathrm{sgs}} = \frac{\nu_{\mathrm{sgs}}}{\mathrm{Pr}_{\mathrm{sgs}}}, \tag{9}$$

where $C_{\rm w} = 0.5$, and $\widetilde{s}^{\rm d}_{ij}$ is the traceless symmetric part of the square of the resolved velocity gradient tensor $\widetilde{g}_{ij} = \partial\widetilde{u}_i/\partial x_j$. The sub-grid scale Prandtl number, $\mathrm{Pr}_{\rm sgs}$, is assumed constant and equal to 0.5 [38, 40]. In particular, assuming that the actual resolution of the SD element in computational space is equal to $\Delta = 1/N$, the cutoff length $\Delta_{\rm g}$ can be evaluated as [15]

$$\Delta_{\rm g}(\boldsymbol{\xi}) \sim \left[\frac{|\det(\boldsymbol{J}(\boldsymbol{\xi}))|}{N^3}\right]^{1/3} = \Delta|\det(\boldsymbol{J}(\boldsymbol{\xi}))|^{1/3}. \tag{10}$$

2.3 Constrained discrete filters for the SD method

When using similarity mixed SGS models, such as the WSM model used in this study, explicit filtering represents a key ingredient to approximate sub-grid scale interactions. This is done by assuming similarity within a narrow band of frequencies in the vicinity of the cutoff frequency characteristic of the mesh. As already mentioned in section 2.2, similarity is assumed between the SGS scales and the smallest resolved scales, which are evaluated as the difference between the filtered and the twice-filtered field. Hence, the explicit filter should be designed (a) to have sufficient localization in physical space; (b) to ensure a certain selected cutoff length-scale. For instance, the box filter in physical space is generally used due to its locality and easy of implementation [19, 37]. Lodato et al. [19], in particular, used a discrete approximation with cutoff length-scale $\Delta_{\rm c} = 4/3\Delta$ according to what was proposed by Akhavan et al. [33], this filter width being an optimal size in order to sufficiently isolate the smallest resolved scales. In the present study, a slightly higher—yet providing sufficient localization in physical space—value of 1.5Δ is adopted.

In order to develop a mixed similarity formulation to be applied with the SD method, the above ideas need to be generalized in a way which is numerically consistent with the use of SD elements. In particular, since the SGS model terms are evaluated at the flux points, the filtered quantities needs to be evaluated at the same flux points starting from the discrete solution at the solution points. This can be achieved by filtering the solution at the solution points first, and then extrapolating the filtered quantities at the flux points using the same Lagrange polynomials used to reconstruct the fluxes (cf. Eq. (5)).

Considering for simplicity the one-dimensional SD element depicted schematically in figure 1, a particularly desirable feature in building discrete filters is that the filter stencil does not lie across elements. Moreover, the non-uniform spacing of the solution points should be taken into account. The above considerations lead to the particularly challenging task of designing asymmetric non-uniform discrete filters with a fixed cutoff length-scale.

For the SD element depicted in figure 1, the discrete filter for a generic quantity ϕ is defined as [41]

$$\overline{\phi}_s = \sum_{i=1}^{N} w_i^s \phi_i, \quad (s = 1, \ldots, N), \tag{11}$$

where the s index refers to a quantity at the N solution points. For the case of hexahedral elements as in the present study, the generalization to three dimensions follows immediately by tensor product of 1D filtering operators.

The spectral signature of the above discrete filter is characterized by its associated transfer function in Fourier space [42], which is readily obtained as

$$\widehat{G}_s(k) = \sum_{i=1}^{N} w_i^s \exp(-\mathrm{j}\beta_i^s k\Delta), \quad \text{with} \quad \beta_i^s = \frac{\xi_i - \xi_s}{\Delta}, \tag{12}$$

where k is the wavenumber and $\mathrm{j} = \sqrt{-1}$; ξ_s represents the location of the solution points, whereas $\Delta = 1/N$ is assumed to be the actual resolution within the SD element (cf. Eq. (10)).

A possible strategy to build discrete filters can be devised by exploiting the resolution properties of polynomials of different order, thus performing the explicit filtering operation by applying the Restriction-Prolongation (RP) technique in each computational cell [10, 43]. Based on Eq. (12), for instance, the real part of the Fourier transform of the discrete filters constructed using the Restriction-Prolongation (RP) technique [10] for $N = 3$ and 4 is plotted in figure 2(a, b), where the Gaussian filter, with cutoff length equal to 1.5Δ, is also represented for reference. As it is immediately evident, the cutoff frequency, viz.,

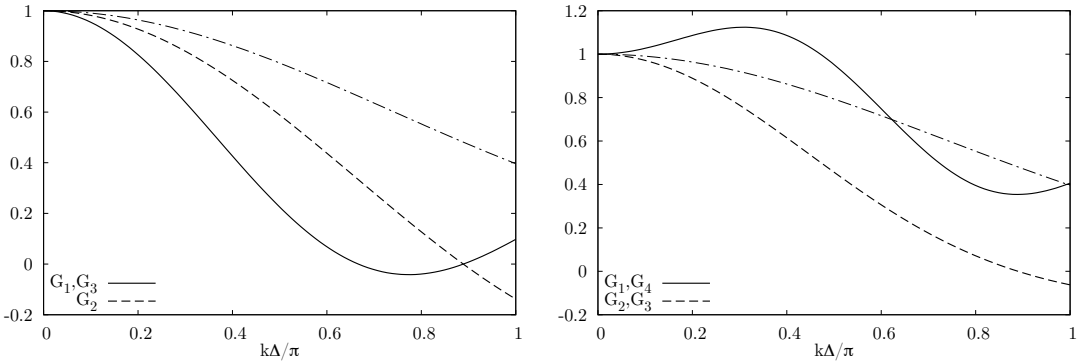

(a) RP filter, $N = 3$ (b) RP filter, $N = 4$

(c) CD filter, $N = 3$ (d) CD filter, $N = 4$

Figure 2: Real part of the transfer function $\widehat{G}(k\Delta/\pi)$ of RP [10] and CD filters for different SD discretization orders N (—·— , analytical Gaussian filter; vertical line: cutoff length-scale at 1.5Δ).

the frequency at which $\widehat{G}_s(k) \simeq 0.5$, for each solution point is different and thus the overall effective cutoff frequency is unpredictable. Furthermore, for $N = 4$, the most asymmetric filters, i.e., those represented with solid lines, have a relatively pronounced over-shoot in the low frequency range, a feature which may lead to non-physical growth of energy. [41]

In order to overcome these problems, a Constrained Discrete (CD) filter satisfying a selected set of conditions, were developed for the SD method. The method used to derive these CD filters is based on the work of Vasilyev et al. [41]. In particular, starting from Eq. (12), the N filter weights w_i^s for the s-th solution point can be determined by providing N constraints. More precisely, a first obvious condition is related to the preservation of a constant variable, namely $\sum_{i=1}^{N} w_i^s = 1$. Then, starting from the idea of building filters whose kernels are as close as possible to that characterizing the Gaussian filter of width $\Delta_c = \alpha\Delta$, the condition

$$\mathrm{Re}[\widehat{G}_s(k_c)] = \sum_{i=1}^{N} w_i^s \cos(\beta_i^s k_c \Delta) = \exp\left(\frac{-\Delta_c^2 k^2}{4\gamma}\right)\Big|_{k=k_c} = \exp(-\pi^2/24), \tag{13}$$

is enforced, with $k_c = \pi/\Delta_c$, therefore constraining the relevant cutoff length-scale. The remaining conditions are obtained by constraining the discrete filter to have $N - 2$ vanishing moments, thus achieving formal commutation with difference operators. [41]

The real part of the kernels of these CD filters for SD elements of order 3 and 4 are plotted in figure 2(c, d). As it can be observed, these CD filters approximate the reference filter much more accurately than the RP filters in the low frequency range, showing more pronounced deviations only at length-scales close to Δ (i.e. $k\Delta/\pi \to 1$). However, recalling that $\Delta \sim O(1/N)$, these small scales are not expected to play a significant role as they are supposedly not supported by the actual resolution of the SD element. The actual

	Re_τ	Re_c	$L_x \times L_y \times L_z$	$n_x \times n_y \times n_z$	N	DoF	Δ_x^+	Δ_y^+	Δ_z^+
CHN1	180	3 440	$4\pi\delta \times 2\delta \times 2\pi\delta$	$15 \times 15 \times 15$	4	216 000	38	2.0–10	19
CHN2	180	3 440	$4\pi\delta \times 2\delta \times 2\pi\delta$	$12 \times 12 \times 12$	5	216 000	38	2.0–10	19
CHN3	395	8 106	$2\pi\delta \times 2\delta \times 1\pi\delta$	$16 \times 12 \times 12$	4	147 456	39	1.2–43	26
CHN4	395	8 106	$2\pi\delta \times 2\delta \times 1\pi\delta$	$13 \times 9 \times 9$	5	131 625	38	2.1–33	28

Table 1: Grid size and resolution for channel flow computations (resolution is estimated as the element size divided by the number of solution points). DoF = $(n_x \times n_y \times n_z) \times N^3$ is the total number of degrees of freedom.

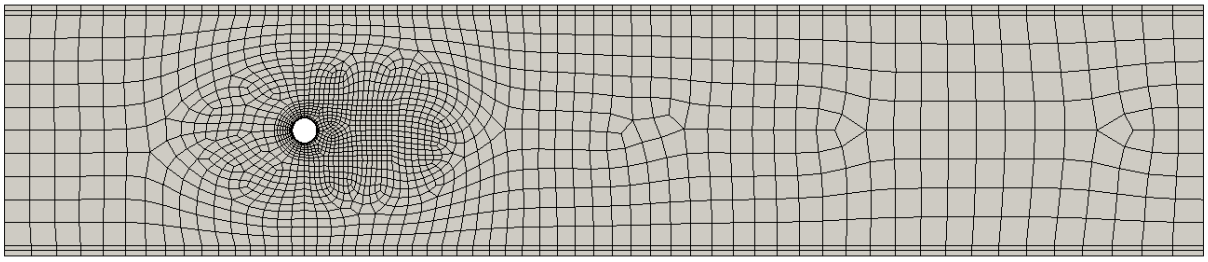

Figure 3: Lateral view of the computational mesh for the circular cylinder in crossflow: 18 470 elements (5×10^5 DoF @ $N = 3$); $-12D$ to $36D$ streamwise, $-5D$ to $5D$ vertical, $-1.6D$ to $1.6D$ spanwise; the cylinder, of diameter D, is centered at the origin.

cutoff frequency is also more predictable throughout the SD element. Moreover, the over-shoots observed in the asymmetric filters constructed by the RP method, are now completely suppressed, hence a better numerical behavior in terms of stability is expected.

3 Results and discussion

In this section, the results obtained with the actual implementation WSM model are presented. Computations on three different geometries are reported: (a) channel flow at Reynolds numbers of 180 and 395 (based on the friction velocity and channel half-width); (b) flow past a confined circular cylinder at Reynolds number 2 580 (based on the upstream bulk velocity and cylinder diameter); (c) flow past a square cylinder at Reynolds number 21 400 (based on the upstream bulk velocity and cylinder side). For comparison, implicit LES computations without the SGS model were performed for the first two geometries.

3.1 Turbulent channel flow

Two channel flow computations were performed at different orders ($N = 4$ and 5) at $Re_\tau = 180$ and 395 (based on the friction velocity u_τ and channel half-width δ), and Mach number 0.3. Grid dimensions and resolutions for the computations are summarized in table 1. Note that the resolution of the computation was estimated as the actual element size divided by the number of solution points used within the element; in a Finite Volume (FV) context, this is equivalent to assuming that each element is filled with N^3 control volumes.

All the computations were performed with periodic boundary conditions in the streamwise and spanwise directions and no-slip isothermal walls were used on the top and bottom planes. In order to drive the flow, a source term $\mathcal{S}$ was added to the x_1 component of momentum. Given the compressible nature of the solver, in particular, $\mathcal{S}$ was determined at each time-step in order to equilibrate the instantaneous resultant shear at the wall, plus a relaxation term toward the expected mass flow rate to accelerate convergence. For consistency, another source term, computed using the bulk velocity as $u_\mathrm{b}\mathcal{S}$, was also added to the energy equation (isothermal walls were used to prevent the energy from increasing without bounds).

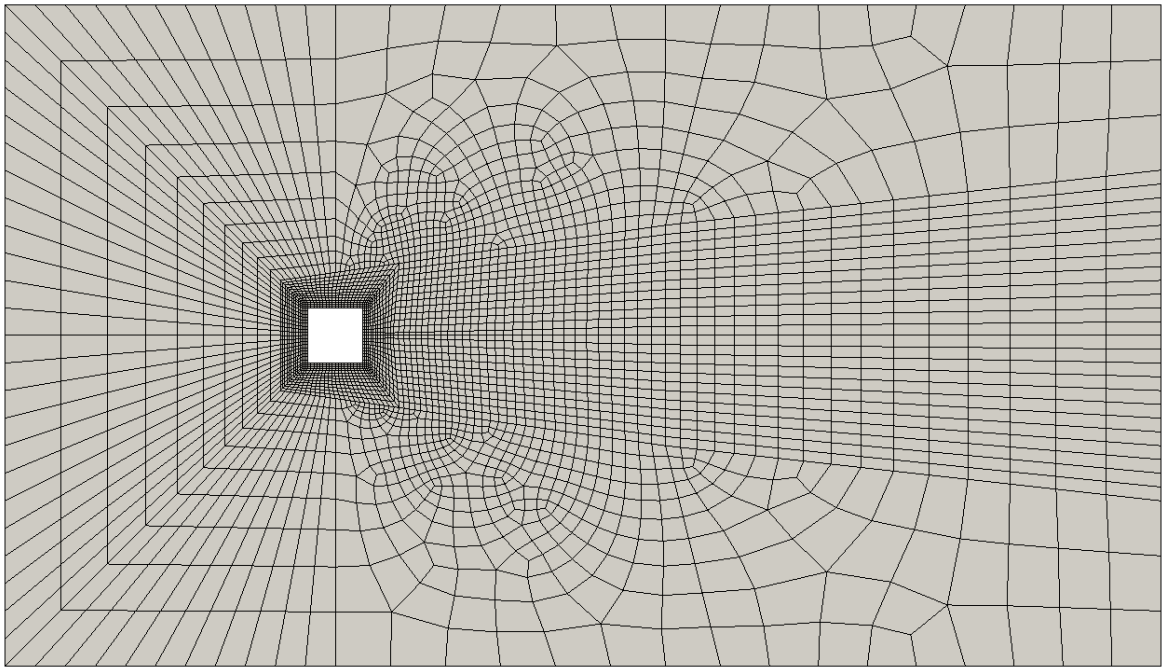

Figure 4: Lateral view of the computational mesh for the square cylinder in crossflow: 35 760 elements (2.3×10^6 DoF @ $N = 4$); $-6D$ to $15D$ streamwise, $-6D$ to $6D$ vertical, $-1.6D$ to $1.6D$ spanwise; the cylinder, of side D, is centered at the origin.

The computations were initialized with a uniform streamwise 4th-order velocity profile

$$u_1(\boldsymbol{x}) = \tfrac{15}{8} u_0 \left[1 - (x_2/\delta)^2\right]^2$$

(u_0 is the reference velocity) and a perturbed vertical velocity component [44, 45]. After the flow field was fully developed and established, time averaging was performed for a period corresponding to about 20 flow-through times; further ensemble averaging in the streamwise and spanwise directions was also performed.

First- and second-order statistical moments are plotted in figures 5–7, where the the results from the explicit LES with the WSM model and the implicit LES are compared to the results from the Direct Numerical Simulations (DNS) performed by Moser et al. [46]. Note that the extremely small density variation ($\sim 1.4\%$ increase from centerline to the wall) did not make it necessary to use the Van Driest correction [47].

The behavior of the WSM model in reproducing the statistical features of the flow is quite satisfactory for each test case. With regards to the mean velocity profiles, the slope of the log law is correctly represented, whereas its intercept is slightly overestimated with respect to the DNS value. The higher order computation gives results in better agreement with the DNS data, even if the DoF and spatial resolution are the same. Overall, the use of the SGS model determines an improvement in the results obtained by implicit LES, which is more evident for the computations with four solution points per element. Reynolds stresses (cf. figure 6) are more sensitive to the use of the SGS model.

With regards to the root mean square (RMS) of the resolved velocity fluctuations, in particular, the profiles obtained with the use of the WSM model are in good agreement with the DNS data, regardless of the spatial discretization order, whereas the implicit LES shows some dependence to the order of the computation. The location and intensity of the peak of streamwise velocity fluctuation is correctly captured. Spanwise and vertical fluctuations tends to be slightly underestimated. Also shown in figures 6 and 7 for the case CHN3 is the curve obtained when the model term is computed using the RP filter. The results in this case show a marked oscillatory behavior with spurious peaks at the location of the element interfaces. This behavior is probably due to the over-shoots observed in the asymmetric filters constructed by the RP

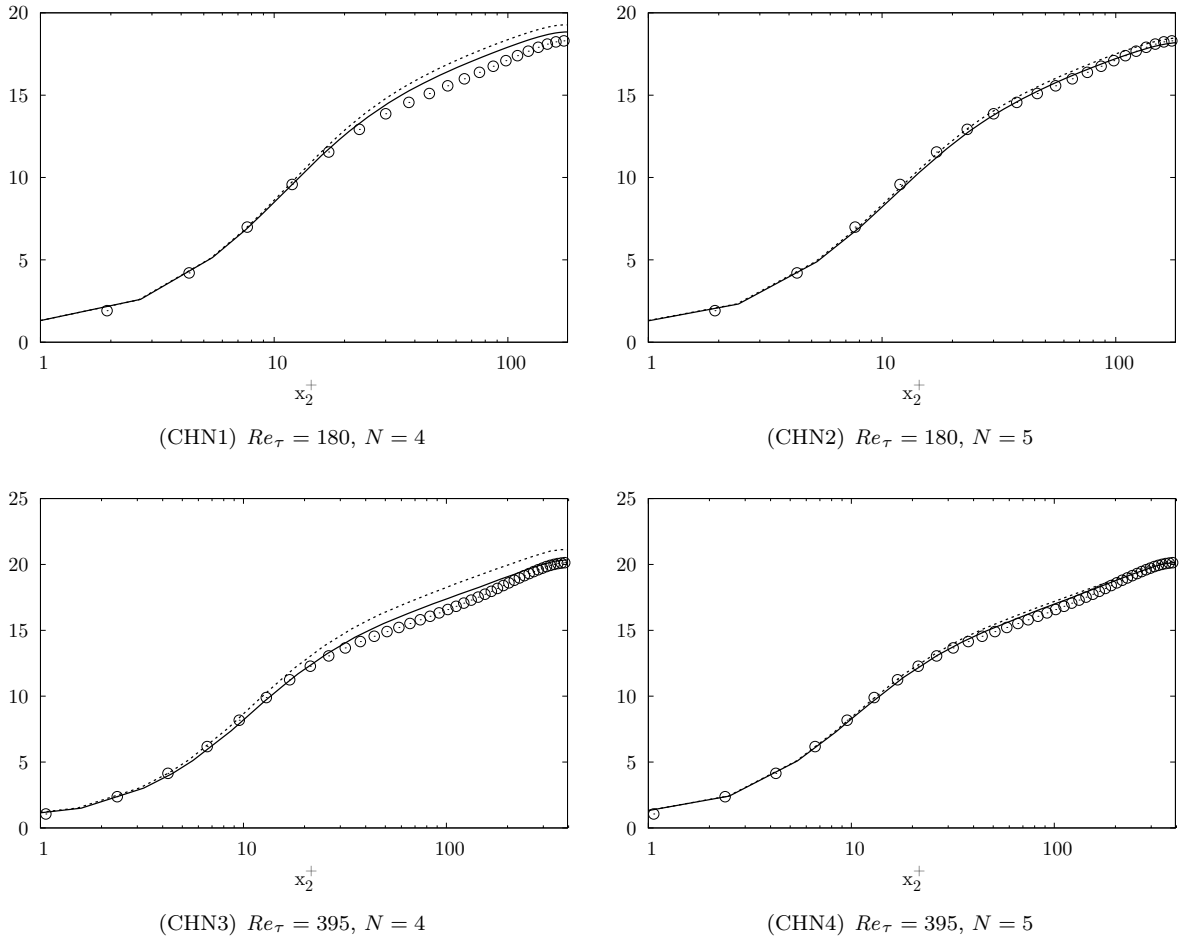

(CHN1) $Re_\tau = 180$, $N = 4$

(CHN2) $Re_\tau = 180$, $N = 5$

(CHN3) $Re_\tau = 395$, $N = 4$

(CHN4) $Re_\tau = 395$, $N = 5$

Figure 5: Mean streamwise velocity profile U^+: ——— , WSM model; ····· , no SGS model; ∘ , DNS data [46].

method for $N = 4$ (cf. figure 2(b), solid line curve).

The resolved turbulent shear stresses from the LES are always below the DNS curves, whereas the results from implicit LES are much closer (cf. figure 7). Given the close connection between the mean streamwise velocity profile and the turbulent shear stress across the channel—the two quantities are strictly related through the steady Reynolds averaged x_1 momentum equation—and given the good agreement observed for the former quantity, it is here argued that the actual global turbulent shear from LES, viz. resolved + SGS modeled contribution, is in good agreement with its DNS counterpart. This is readily confirmed by collecting the mean SGS shear stress $\langle \tau_{12} \rangle$ during the computation and by comparing the *exact* turbulent shear from DNS with the approximate global (resolved + SGS) turbulent shear from LES, viz. $\langle \overline{u}_1' \overline{u}_2' \rangle + \langle \tau_{12} \rangle$ [48]. As it can be observed in figure 7, the approximate global turbulent shear matches almost perfectly the DNS data, thus confirming that the model is correctly compensating the insufficient shear from the resolved flow field.

3.2 Flow past a circular cylinder

The simulations, an implicit LES and an explicit LES with the WSM model and the new discrete filter, were performed at Reynolds and Mach numbers of 2 580 and 0.25, respectively, based on the bulk velocity at the inlet U_b and the cylinder diameter D. The equations were integrated over an unstructured computational mesh of dimension $48D \times 10D \times 3.2D$ (L×H×W) with 18 470 unstructured hexahedral elements, and $N = 3$ (cf. figure 3). Therefore, the number of DoF was equal to 498 690. Note that, compared to the resolution of the structured coarse mesh used by Mohammad et al. [12] for a similar LES computation, the resolution

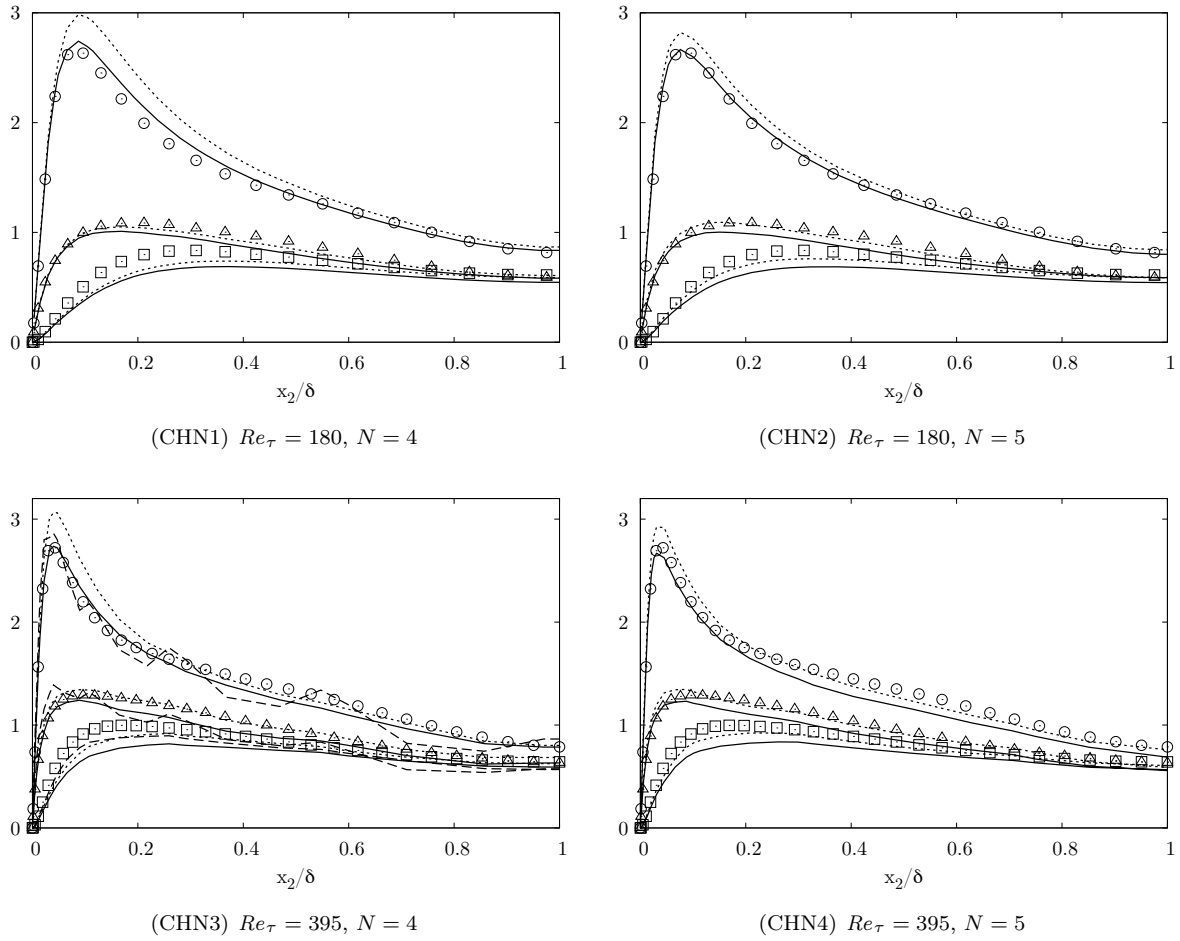

(CHN1) $Re_\tau = 180$, $N = 4$ (CHN2) $Re_\tau = 180$, $N = 5$

(CHN3) $Re_\tau = 395$, $N = 4$ (CHN4) $Re_\tau = 395$, $N = 5$

Figure 6: RMS of velocity fluctuations: ——— , WSM model (CD filter); ----- , WSM model (RP filter); ····· , no SGS model; symbols, DNS data [46]. ○ , $u^+_{\rm rms}$; □ , $v^+_{\rm rms}$; △ , $w^+_{\rm rms}$.

adopted here is about 5 times lower. Such a low resolution was used to assess the performances of the SGS model and the relevant discrete filters in a case in which the implicit LES is almost certainly expected to fail. The boundary conditions were periodic in the spanwise direction and no-slip adiabatic conditions were used on the top and bottom planes; the cylinder wall was set as no-slip adiabatic as well and the inflow/outflow conditions were imposed fixing the inlet density and velocity and the outlet pressure, respectively. After the flow field was fully developed and established, statistics were performed averaging in time for about 300 shedding periods, which, according to Parnaudeau et al. [51], represents a long enough sample in order for statistics to be fully converged; in view of the statistical two-dimensionality of the flow field, further ensemble averaging in the spanwise direction was also performed. Results were compared against Particle Image Velocimetry (PIV) experimental measurements [49, 50].

First- and second-order statistical moments at different locations behind the cylinder, and along the wake, are plotted in figures 8 and 9. Despite the extremely low resolution adopted, average profiles obtained using the SGS model are in very good agreement with the experimental data. The recirculation length, an extremely sensitive parameter for this kind of flow configuration, is well captured as well (cf. the mean velocity inversion point in figure 9). The computation without the SGS model, as expected, does not perform well. Significant deviations from the experimental data are observed, and the recirculation length is over predicted of about 20%.

With regards to the second-order statistical moments, results are not fully satisfactory even when the SGS model is used. Even though some improvement over the implicit LES is observed for $x/D \geq 2$, it is

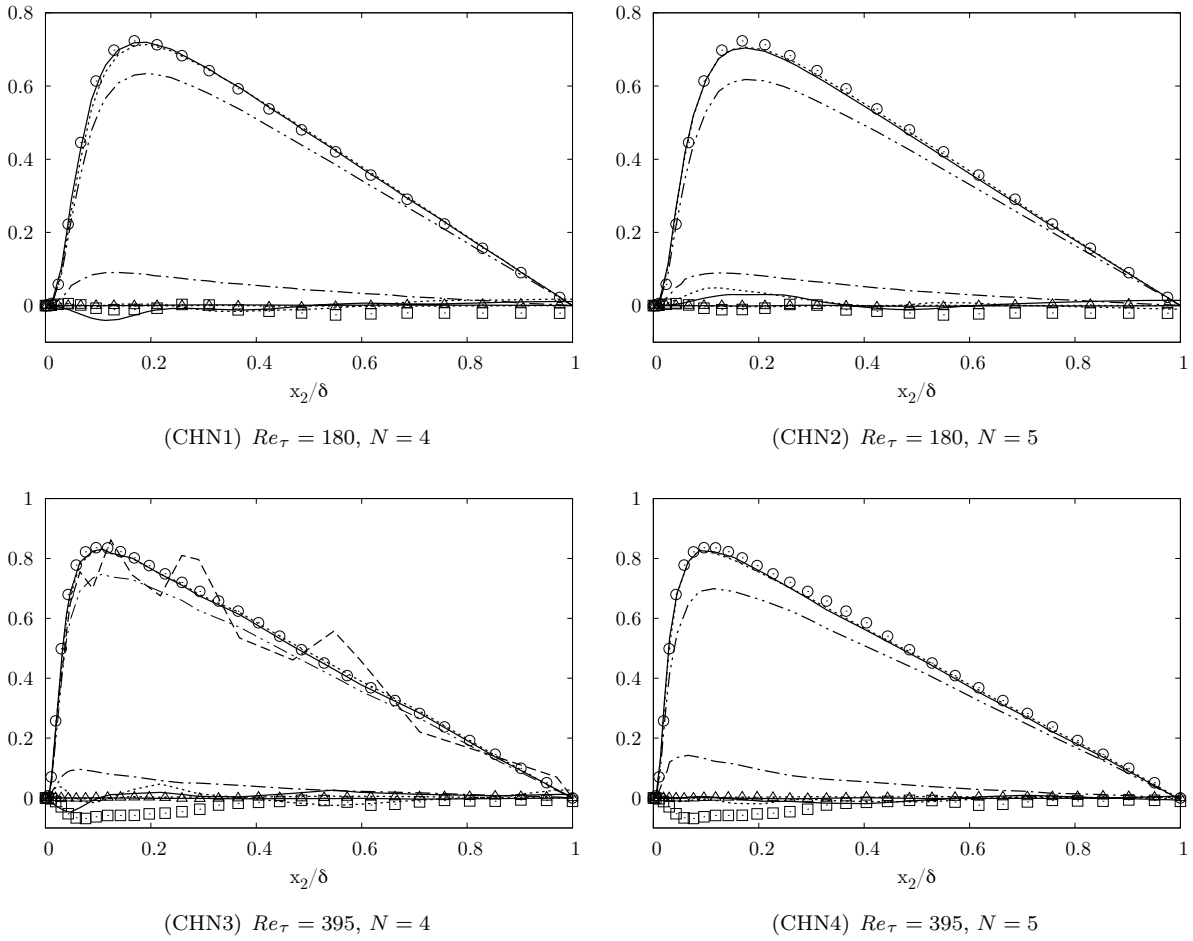

(CHN1) $Re_\tau = 180$, $N = 4$ (CHN2) $Re_\tau = 180$, $N = 5$

(CHN3) $Re_\tau = 395$, $N = 4$ (CHN4) $Re_\tau = 395$, $N = 5$

Figure 7: Reynolds shear stresses: ——— , WSM model with CD filter (resolved + SGS); – – – – – , WSM model with RP filter; ····· , no SGS model; —·— , $\langle \tau_{12} \rangle$ from LES; —··— resolved shear stress from LES (CD filter); symbols, DNS data [46]. ∘ , $-\langle u^+ v^+ \rangle$; □ , $-\langle u^+ w^+ \rangle$; △ , $-\langle v^+ w^+ \rangle$.

difficult to judge which computation is performing better. Grid resolution is clearly too low for the model used to be able to correctly reproduce also the Reynolds stresses. Further tests are under way using more suitable resolutions of 1.2×10^6 and 2.3×10^6 DoF (i.e. $N = 4$ and 5, respectively).

3.3 Flow past a square cylinder

An explicit LES with the WSM model and the new discrete filter was performed at Reynolds and Mach numbers of 21 400 and 0.3, respectively, based on the bulk velocity at the inlet U_b and the cylinder diameter D. The computation was set up in order to replicate the experiment described in Refs. [52, 53], for which Laser-Doppler Velocimetry (LDV) experimental measurements are available. The equations were integrated over an unstructured computational mesh of dimension $21D \times 12D \times 3.2D$ (L×H×W) with 35 760 unstructured hexahedral elements, and $N = 4$ (cf. figure 4). Therefore, the number of DoF was equal to 2.3×10^6. Overall grid resolution for the selected Reynolds numbers can be considered as relatively low, as is substantiated by the high values measured for the instantaneous normalized SGS energy transfer coefficient $\nu_\mathrm{ratio} = \tau_{ij}^\mathrm{d} \widetilde{A}_{ij} / 2\overline{\mu} \widetilde{A}_{ij} \widetilde{A}_{ij}$ [19] in figure 10. For such values of ν_ratio, the sub-grid activity parameter [54] can be reasonably expected to be in the range 0.5–1. The boundary conditions were periodic in the spanwise direction and no-slip isothermal conditions were used on the cylinder walls; the inflow/outflow conditions were imposed fixing the inlet density and velocity and the outlet pressure, respectively. After the flow field was fully developed and established, statistics were performed averaging in time for about 16 shedding pe-

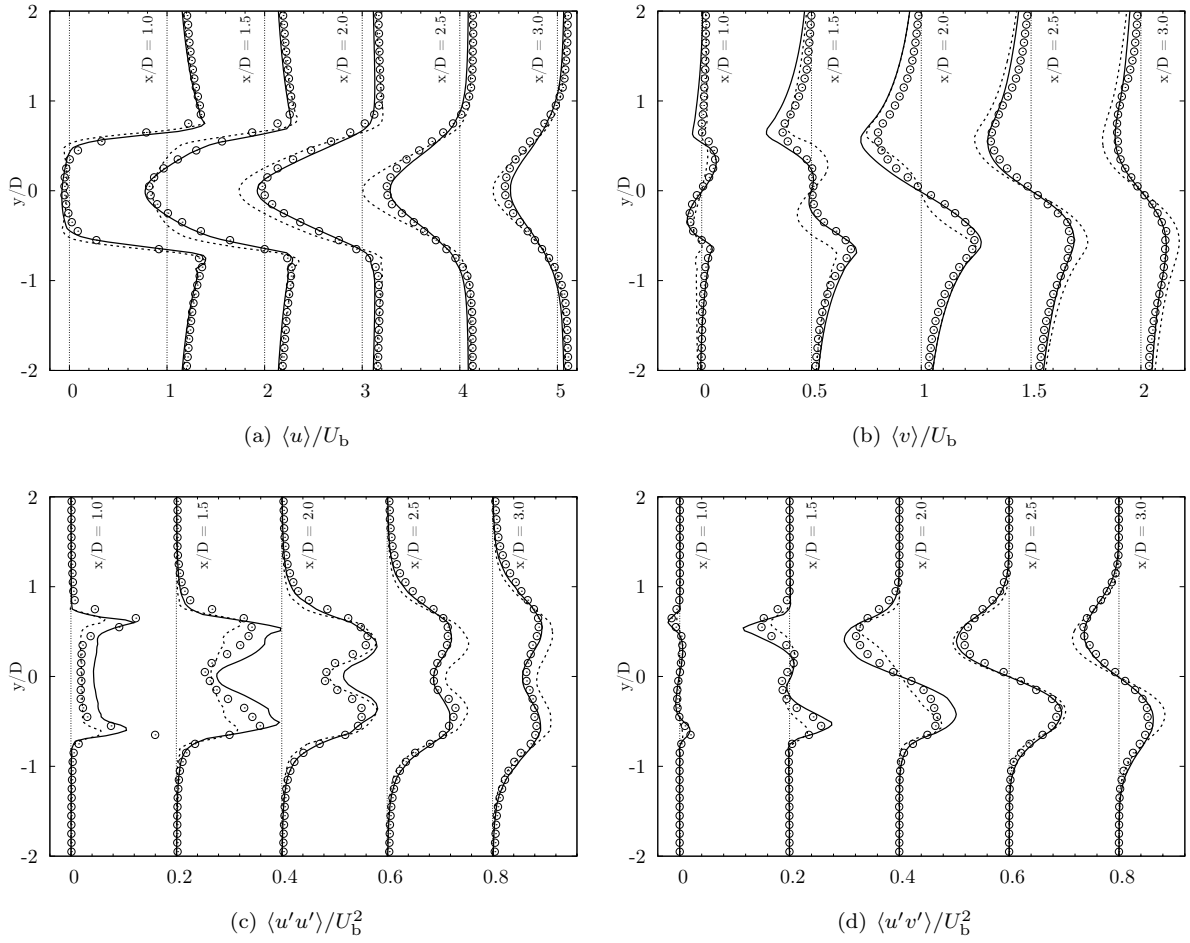

(a) $\langle u \rangle / U_\mathrm{b}$ (b) $\langle v \rangle / U_\mathrm{b}$

(c) $\langle u'u' \rangle / U_\mathrm{b}^2$ (d) $\langle u'v' \rangle / U_\mathrm{b}^2$

Figure 8: First- and second-order statistical moments of the resolved velocity field at different locations downstream of the cylinder: ——— , WSM model; ····· , no SGS model; ∘ , experimental PIV measurements [49, 50] (every two points represented). Light dotted lines represent the zero location of the shifted curves.

riods, which for this Reynolds number provided relatively well converged statistical samples; in view of the statistical two-dimensionality of the flow field, further ensemble averaging in the spanwise direction was also performed.

First- and second-order statistical moments at different locations behind the cylinder are plotted in figure 11. Both the average profiles and the Reynolds stresses obtained using the implemented WSM model using the new filter are in extremely good agreement with the experimental data. As a further validation of the computation, the discrete Fourier transform of the time history of the lift coefficient (see figure 12) returned a shedding Strouhal number of 0.130, which is in very good agreement with the experimental counterpart, i.e., $St = 0.132 \pm 0.004$ [53].

4 Concluding remarks

Overall, the performance of the actual WSM model implementation in conjunction with the SD method and the new discrete filters is extremely satisfactory. In all the flow configurations studied, statistical moments extracted from LES were in very good agreement with DNS and experimental data. For the test cases where a comparison was done with results from implicit LES (i.e., turbulent channel flow and flow past a circular cylinder), results were generally improved when the SGS model was active.

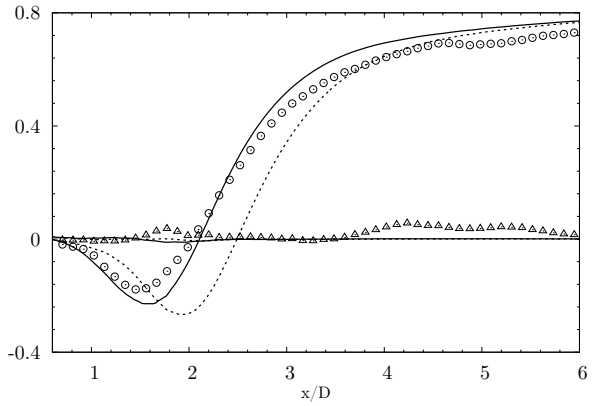

Figure 9: Streamwise and vertical average velocity measured along the wake of the cylinder at $y/D = 0$: ——— , WSM model; ····· , no SGS model; symbols ($\circ$, streamwise; $\triangle$, vertical), experimental PIV measurements [49, 50] (every two points represented).

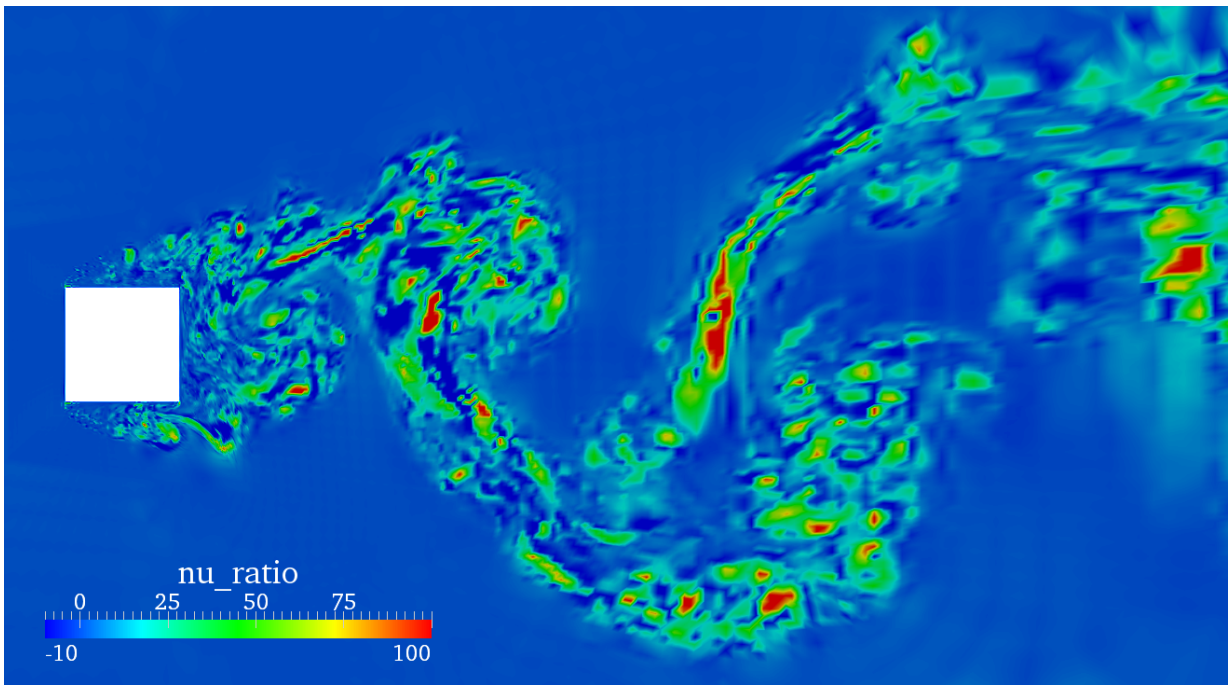

Figure 10: Instantaneous contours of the normalized SGS energy transfer coefficient ν_{ratio}.

Depending on the grid resolution, the benefits resulting from using the SGS model are of different nature. First-order statistical moments are significantly improved, the improvement being especially evident in the case of relatively under-resolved LES computations, where the implicit LES cannot be expected to give satisfactory results. More challenging is, of course, to reproduce second-order statistical moments which, in order to be correctly captured, still need the grid to resolve enough turbulent kinetic energy. For sufficiently resolved computations, improvements in the Reynolds stresses were observed when the WSM model was turned on, whereas in the case of coarse LES computations, the improvements were more subtle. In any case, turbulent shear stresses are generally well captured by the proposed implementation of the WSM model.

The proposed constrained discrete filters of arbitrary order, in particular, proved to be numerically stable at any tested order (up to $N = 7$ in other tests not included here) and allow a relatively straightforward implementation into high-order SD schemes (or any other discontinuous finite element numerical method)

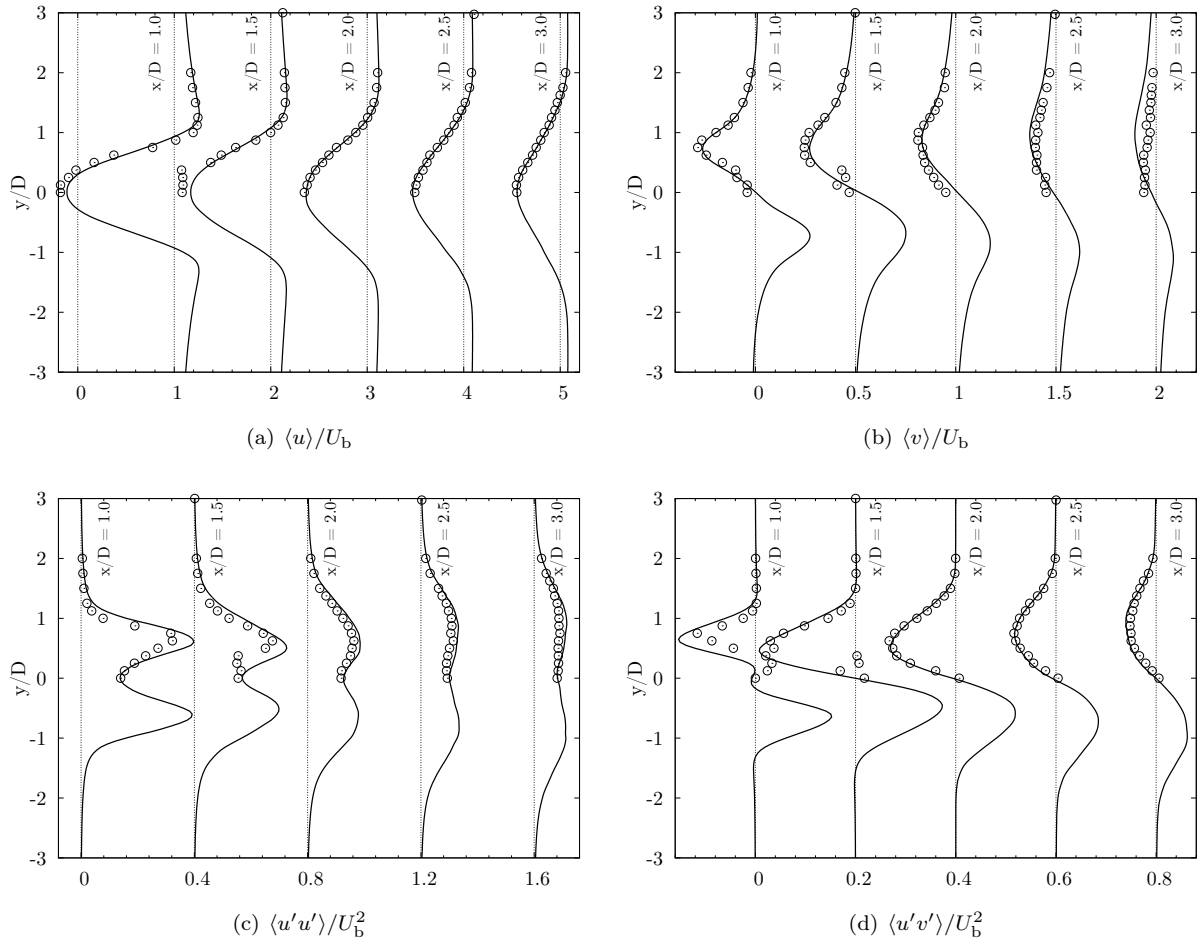

Figure 11: First- and second-order statistical moments of the resolved velocity field at different locations downstream of the square cylinder: ——— , WSM model; ∘ , experimental LDV measurements [52, 53]. Light dotted lines represent the zero location of the shifted curves.

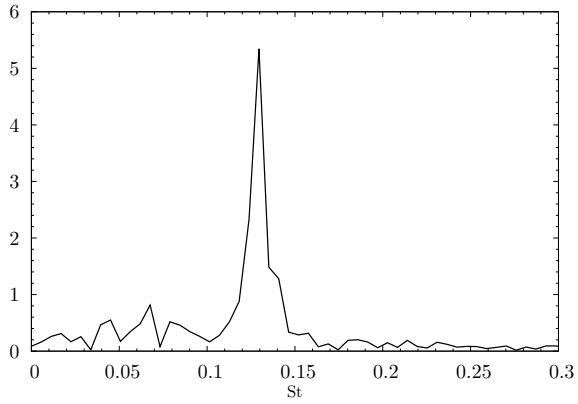

Figure 12: Discrete Fourier transform of the time history of the lift coefficient.

of any SGS model which relies upon the use of explicit filtering or dynamic procedures [55, 56]. For the similarity mixed formulation used in the present study, in particular, existing filtering approaches based on

solution projection over low-order polynomial bases proved to be inadequate, and keen to develop spurious numerical artifacts at the elements interfaces. In the tests performed, the newly developed discrete filters did not lead to any similar unexpected and unphysical behavior throughout the computational domain. Further development of wall modeling procedures and the unstructured nature of the high-order SD scheme will also allow relatively affordable high fidelity LES computations in complex geometries.

Acknowledgements

Financial support under NSF grant No. 0915006 monitored by Dr. Leland Jameson, and AFOSR grant No. FA 9550-07-1-0195 from the Computational Math Program under the direction of Dr. Fariba Fahroo, is gratefully acknowledged.

References

[1] Jan S. Hesthaven and Tim Warburton. *Nodal Discontinuous Galerkin Methods: Algorithms, Analysis, and Applications*. Springer Science+Business Media, LLC, 2008.

[2] G. Karniadakis and S.J. Sherwin. *Spectral/hp element methods for CFD*. Oxford University Press, USA, 1999.

[3] D.A. Kopriva and J.H. Kolias. A conservative staggered-grid Chebyshev multidomain method for compressible flows. *J. Comput. Phys.*, 125(1):244–261, 1996.

[4] H.T. Huynh. A flux reconstruction approach to high-order schemes including discontinuous Galerkin methods. *AIAA P.*, 2007-4079, 2007. 18th AIAA Computational Fluid Dynamics Conference, Miami, FL, Jun. 25–28, 2007.

[5] Y. Liu, M. Vinokur, and Z.J. Wang. Spectral difference method for unstructured grids I: basic formulation. *J. Comput. Phys.*, 216(2):780–801, 2006.

[6] G. May and A. Jameson. A spectral difference method for the Euler and Navier-Stokes equations on unstructured meshes. *AIAA P.*, 2006-304, 2006. 44th AIAA Aerospace Sciences Meeting, Reno, NV, Jan. 9–12, 2006.

[7] Y. Sun, Z.J. Wang, and Y. Liu. High-order multidomain spectral difference method for the Navier-Stokes equations on unstructured hexahedral grids. *Commun. Comput. Phys.*, 2(2):310–333, 2007.

[8] Z.J. Wang, Y. Liu, G. May, and A. Jameson. Spectral difference method for unstructured grids II: Extension to the Euler equations. *J. Sci. Comput.*, 32(1):45–71, 2007.

[9] C. Liang, A. Jameson, and Z.J. Wang. Spectral difference method for compressible flow on unstructured grids with mixed elements. *J. Comput. Phys.*, 228(8):2847–2858, 2009.

[10] S. Premasuthan, C. Liang, and A. Jameson. A Spectral Difference method for viscous compressible flows with shocks. *AIAA P.*, 2009-3785, 2009. 19th AIAA Computational Fluid Dynamics, San Antonio, Texas, Jun. 22-25, 2009, 16 p.

[11] C. Liang, S. Premasuthan, A. Jameson, and Z.J. Wang. Large eddy simulation of compressible turbulent channel flow with spectral difference method. *AIAA P.*, 2009-402, 2009. 47th AIAA Aerospace Sciences Meeting Including The New Horizons Forum and Aerospace Exposition, Orlando, FL, Jan. 5–8, 2009, 15 p.

[12] A.H. Mohammad, Z.J. Wang, and C. Liang. Large eddy simulation of flow over a cylinder using high-order spectral difference method. *Adv. Appl. Math. Mech.*, 2(4):451–466, 2010.

[13] K. Ou, C. Liang, S. Premasuthan, and A. Jameson. High-order spectral difference simulation of laminar compressible flow over two counter-rotating cylinders. *AIAA P.*, 2009-3956, 2009. 27th AIAA Applied Aerodynamics Conference, San Antonio, TX, Jun. 22–25, 2009.

[14] P. Castonguay, C. Liang, and A. Jameson. Simulation of Transitional Flow over Airfoils using the Spectral Difference Method. *AIAA P.*, 2010-4626, 2010.

[15] M. Parsani, G. Ghorbaniasl, C. Lacor, and E. Turkel. An implicit high-order spectral difference approach for large eddy simulation. *J. Comput. Phys.*, 229(14):5373–5393, 2010.

[16] F. Nicoud and F. Ducros. Subgrid-scale stress modelling based on the square of the velocity gradient tensor. *Flow Turbul. Combust.*, 62(3):183–200, September 1999.

[17] M. Parsani, G. Ghorbaniasl, and C. Lacor. Validation and application of an high-order spectral difference method for flow induced noise simulation. *J. Comput. Acoust.*, 19(3):241–268, 2011.

[18] J. Bardina, J.H. Ferziger, and W.C. Reynolds. Improved subgrid-scale models for large-eddy simulation. *AIAA P.*, 1980-1357, July 1980. Fluid and Plasma Dynamics Conference, 13th, Snowmass, CO, Jul. 14-16, 1980, 10 p.

[19] G. Lodato, L. Vervisch, and P. Domingo. A compressible wall-adapting similarity mixed model for Large-Eddy Simulation of the impinging round jet. *Phys. Fluids*, 21(3):035102, 2009.

[20] H.T. Huynh. A reconstruction approach to high-order schemes including discontinuous Galerkin for diffusion. *AIAA P.*, 2009-403, 2009. 47th AIAA Aerospace Sciences Meeting, Orlando, FL, Jan. 5–8, 2009.

[21] A. Jameson. A proof of the stability of the spectral difference method for all orders of accuracy. *J. Sci. Comput.*, 45(1):348–358, 2010.

[22] A. Jameson. Advances in bringing high-order methods to practical applications in computational fluid dynamics. *AIAA P.*, 2011-3226, 2011. 20th AIAA Computational Fluid Dynamics Conference, Honolulu, Hawaii, Jun. 27–30, 2011.

[23] A. Jameson, P.E. Vincent, and P. Castonguay. On the non-linear stability of flux reconstruction schemes. *J. Sci. Comput.*, 50(2):434–445, 2012.

[24] P.E. Vincent, P. Castonguay, and A. Jameson. A new class of high-order energy stable flux reconstruction schemes. *J. Sci. Comput.*, 47(1):1–23, 2010.

[25] P.E. Vincent, P. Castonguay, and A. Jameson. Insights from von Neumann analysis of high-order flux reconstruction schemes. *J. Comput. Phys.*, 230(22):8134–8154, 2011.

[26] P.E. Vincent and A. Jameson. Facilitating the adoption of unstructured high-order methods amongst a wider community of fluid dynamicists. *Math. Model. Nat. Phenom.*, 6(3):97–140, 2011.

[27] D. Williams, P. Castonguay, P.E. Vincent, and A. Jameson. An extension of energy stable flux reconstruction to unsteady, non-linear, viscous problems on mixed grids. *AIAA P.*, 2011-3405:37, 2011. 20th AIAA Computational Fluid Dynamics Conference, Honolulu, Hawaii, Jun. 27–30, 2011.

[28] P. Castonguay, P.E. Vincent, and A. Jameson. A new class of high-order energy stable flux reconstruction schemes for triangular elements. *J. Sci. Comput.*, 51(1):224–256, 2012.

[29] Marcel Lesieur, Olivier Métais, and Pierre Comte. *Large-Eddy Simulations of Turbulence*. Cambridge University Press, 2005.

[30] P.L. Roe. Approximate Riemann solvers, parameter vectors, and difference schemes. *J. Comput. Phys.*, 43:357–372, 1981.

[31] A. Harten. High resolution schemes for hyperbolic conservation laws. *J. Comput. Phys.*, 49(3):357–393, 1983.

[32] S. Liu, C. Meneveau, and J. Katz. On the properties of similarity subgrid-scale models as deduced from measurements in a turbulent jet. *J. Fluid Mech.*, 275:83–119, 1994.

[33] R. Akhavan, A. Ansari, S. Kang, and N. Mangiavacchi. Subgrid-scale interactions in a numerically simulated planar turbulent jet and implications for modeling. *J. Fluid Mech.*, 408:83–120, 2000.

[34] M.V. Salvetti and S. Banerjee. *A priori* tests of a new dynamic subgrid-scale model for finite-difference large-eddy simulations. *Phys. Fluids*, 7(11):2831–2847, November 1995.

[35] R. Anderson and C. Meneveau. Effects of the similarity model in finite-difference LES of isotropic turbulence using a Lagrangian dynamic mixed model. *Flow Turbul. Combust.*, 62(3):201–225, 1999.

[36] T.A. Zang, R.B. Dahlburg, and J.P. Dahlburg. Direct and large-eddy simulations of three-dimensional compressible Navier-Stokes turbulence. *Phys. Fluids A-Fluid*, 4(1):127–140, January 1992.

[37] Yan Zang, Robert L. Street, and Jeffrey R. Koseff. A dynamic mixed subgrid-scale model and its application to turbulent recirculating flows. *Phys. Fluids A-Fluid*, 5(12):3186–3196, December 1993.

[38] G. Erlebacher, M.Y. Hussaini, C.G. Speziale, and T.A. Zang. Toward the large-eddy simulation of compressible turbulent flows. *J. Fluid Mech.*, 238:155–185, 1992.

[39] C.G. Speziale. Galilean invariance of subgrid-scale stress models in the large-eddy simulation of turbulence. *J. Fluid Mech.*, 156:55–62, 1985.

[40] C.G. Speziale, G. Erlebacher, T.A. Zang, and M.Y. Hussaini. The subgrid-scale modeling of compressible turbulence. *Phys. Fluids*, 31(4):940–942, April 1988.

[41] O.V. Vasilyev, T.S. Lund, and P. Moin. A general class of commutative filters for LES in complex geometries. *J. Comput. Phys.*, 146(1):82–104, 1998.

[42] J. Berland, C. Bogey, O. Marsden, and C. Bailly. High-order, low dispersive and low dissipative explicit schemes for multiple-scale and boundary problems. *J. Comput. Phys.*, 224(2):637–662, 2007.

[43] H.M. Blackburn and S. Schmidt. Spectral element filtering techniques for large eddy simulation with dynamic estimation. *J. Comput. Phys.*, 186(2):610–629, 2003.

[44] P. Andersson, L. Brandt, A. Bottaro, and D.S. Henningson. On the breakdown of boundary layer streaks. *J. Fluid Mech.*, 428(1):29–60, 2001.

[45] R. Rossi. Direct numerical simulation of scalar transport using unstructured finite-volume schemes. *J. Comput. Phys.*, 228(5):1639–1657, 2009.

[46] R.D. Moser, J. Kim, and N.N. Mansour. Direct numerical simulation of turbulent channel flow up to $\mathrm{Re}_\tau = 590$. *Phys. Fluids*, 11(4):943–945, April 1999.

[47] H. Foysi, S. Sarkar, and R. Friedrich. Compressibility effects and turbulence scalings in supersonic channel flow. *J. Fluid Mech.*, 509(1):207–216, 2004.

[48] Pierre Sagaut. *Large Eddy Simulation for Incompressible Flows: An Introduction.* Springer-Verlag Berlin Heidelberg, 2 edition, 2001.

[49] E. Konstantinidis, S. Balabani, and M. Yianneskis. The effect of flow perturbations on the near wake characteristics of a circular cylinder. *J. Fluid. Struct.*, 18(3-4):367–386, 2003.

[50] E. Konstantinidis, S. Balabani, and M. Yianneskis. Conditional averaging of PIV plane wake data using a cross-correlation approach. *Exp. Fluids*, 39(1):38–47, 2005.

[51] P. Parnaudeau, J. Carlier, D. Heitz, and E. Lamballais. Experimental and numerical studies of the flow over a circular cylinder at Reynolds number 3900. *Phys. Fluids*, 20:085101, 2008.

[52] D.A. Lyn and W. Rodi. The flapping shear layer formed by flow separation from the forward corner of a square cylinder. *J. Fluid Mech.*, 267:353–376, 1994.

[53] D.A. Lyn, S. Einav, W. Rodi, and J.H. Park. A laser-Doppler velocimetry study of ensemble-averaged characteristics of the turbulent near wake of a square cylinder. *J. Fluid Mech.*, 304(1):285–319, 1995.

[54] B.J. Geurts and J. Fröhlich. A framework for predicting accuracy limitations in large-eddy simulation. *Phys. Fluids*, 14(6):L41–L44, 2002.

[55] M. Germano, U. Piomelli, P. Moin, and W.H. Cabot. A dynamic subgrid-scale eddy viscosity model. *Phys. Fluids A-Fluid*, 3(7):1760–1765, July 1991.

[56] P. Moin, K. Squires, W. Cabot, and S. Lee. A dynamic subgrid-scale model for compressible turbulence and scalar transport. *Phys. Fluids A-Fluid*, 3(11):2746–2757, November 1991.